



Cite as
Nano-Micro Lett.
(2020) 12:172

Received: 9 June 2020
Accepted: 28 July 2020
© The Author(s) 2020

Plasmonic Ag-Decorated Few-Layer MoS₂ Nanosheets Vertically Grown on Graphene for Efficient Photoelectrochemical Water Splitting

Dong-Bum Seo¹, Tran Nam Trung¹, Dong-Ok Kim¹, Duong Viet Duc¹, Sungmin Hong², Youngku Sohn², Jong-Ryul Jeong¹, Eui-Tae Kim¹ ✉

✉ Eui-Tae Kim, etkim@cnu.ac.kr

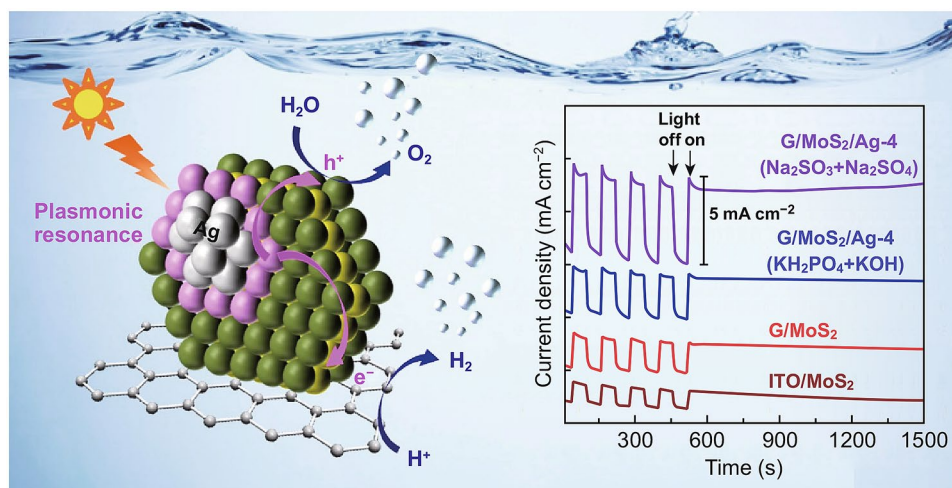
¹ Department of Materials Science and Engineering, Chungnam National University, Daejeon 34134, Republic of Korea

² Department of Chemistry, Chungnam National University, Daejeon 34134, Republic of Korea

HIGHLIGHTS

- Controllable and large-scale practical growth of plasmonic Ag-decorated vertically aligned 2D MoS₂ nanosheets on graphene.
- Realization of the synergistic effects of surface plasmon resonance and favorable graphene/MoS₂ heterojunction to enhance the photoelectrochemical reactivity of 2D MoS₂.

ABSTRACT A controllable approach that combines surface plasmon resonance and two-dimensional (2D) graphene/MoS₂ heterojunction has not been implemented despite its potential for efficient photoelectrochemical (PEC) water splitting. In this study, plasmonic Ag-decorated 2D MoS₂ nanosheets were vertically grown on graphene substrates in a practical large-scale manner through metalorganic chemical vapor deposition of MoS₂ and thermal evaporation of Ag. The plasmonic Ag-decorated MoS₂ nanosheets on graphene yielded up to 10 times higher photo-to-dark current ratio than MoS₂ nanosheets on indium tin oxide. The significantly enhanced PEC activity could be attributed to the synergistic effects of SPR and favorable graphene/2D MoS₂ heterojunction. Plasmonic Ag nanoparticles not only increased visible-light and near-infrared absorption of 2D MoS₂, but also induced highly amplified local electric field intensity in 2D MoS₂. In addition, the vertically aligned 2D MoS₂ on graphene acted as a desirable heterostructure for efficient separation and transportation of photo-generated carriers. This study provides a promising path for exploiting the full potential of 2D MoS₂ for practical large-scale and efficient PEC water-splitting applications.



The significantly enhanced PEC activity could be attributed to the synergistic effects of SPR and favorable graphene/2D MoS₂ heterojunction. Plasmonic Ag nanoparticles not only increased visible-light and near-infrared absorption of 2D MoS₂, but also induced highly amplified local electric field intensity in 2D MoS₂. In addition, the vertically aligned 2D MoS₂ on graphene acted as a desirable heterostructure for efficient separation and transportation of photo-generated carriers. This study provides a promising path for exploiting the full potential of 2D MoS₂ for practical large-scale and efficient PEC water-splitting applications.

KEYWORDS Photoelectrocatalysis; Molybdenum disulfide; Graphene; Surface plasmon resonance



1 Introduction

Photoelectrochemistry (PEC) and photocatalysis of semiconductors have been extensively studied as effective approaches for energy conversion, such as hydrogen gas production by water splitting, and for environmental applications, such as air/water purification, water disinfection, and hazardous waste remediation [1–7]. Recently, two-dimensional (2D) layered MoS₂ has attracted considerable research attention as a promising semiconductor photocatalyst because of its excellent catalytic activity, high chemical stability, eco-friendliness, and abundance in nature [2–4]. In particular, few-layer-thick MoS₂ nanosheets can be central to exploiting the full potential of 2D MoS₂ for solar-light PEC reactions because of the feasibility of mass production and appropriate bandgap energy, which is tunable from ~1.2 eV for indirect gap in the bulk form to ~1.9 eV for direct gap in the monolayer [8–10]. The PEC activity of 2D MoS₂, which has strong in-plane covalent bonding of S–Mo–S and weak out-of-plane van der Waals interaction between neighboring S–S layers, is significantly hindered by poor charge transport across basal layers through hopping [2–4]. Thus, the ideal architecture configuration comprises 2D MoS₂ nanosheets that stand vertically on electrode substrates because the highly conductive edges of MoS₂ provide an efficient pathway for photoexcited carriers and good electronic contact with the substrate. In addition, vertically packed 2D sheets offer higher volume than laid sheets for interacting with incoming photon flux on a unit substrate area. He et al. demonstrated that the edge-on structure of MoS₂ flakes/TiO₂ nanowires improves the photocatalytic hydrogen evolution of MoS₂ [11]. Recently, we reported the enhanced PEC activity of few-layer MoS₂ nanosheets vertically grown on supporting electrode substrates, such as indium-tin oxide (ITO) and ITO/TiO₂ nanowires [12, 13]. However, the synthesis and PEC applications of vertically aligned few-layer MoS₂ nanosheets on graphene have not been reported despite its considerable potential.

The support substrate should be made highly conductive and form an appropriate energy band alignment with MoS₂ to minimize Ohmic junction losses. Graphene has attracted huge research attention as a promising conducting layer not only because it displays remarkable electron mobility (> 15,000 cm² V⁻¹ s⁻¹) but also due to its favorable electric contact with MoS₂. Chang et al. reported the enhanced

photocatalytic hydrogen evolution of MoS₂/graphene as a result of the improved charge transport of graphene [14]. Carraro et al. demonstrated the one-pot aerosol synthesis of MoS₂ nanoparticles/graphene for enhanced PEC hydrogen production [15]. Biroju et al. also reported that an adequate stacking of 2D MoS₂ and graphene exhibited a ΔG_{H} value that is close to zero, which is ideal for hydrogen evolution reactions [16]. However, most MoS₂/graphene heterostructures have been synthesized by wet-chemical and mechanical transfer approaches, which are unsuitable for controlled synthesis or vertical stacking of few-layer MoS₂ nanosheets on graphene electrode substrates [14–18]. Wet-chemical synthesis methods have yielded a wide range of MoS₂ layer thicknesses and produced the randomly assembled structures of 2D MoS₂ and graphene [14, 15, 19].

The optical absorption of 2D MoS₂ can be remarkably enhanced by employing plasmonic metal nanoparticles (NPs), such as Ag or Au. Plasmonic metals improve the optical absorption over the entire solar spectrum as well as broaden and tune the optical absorption behavior, depending on their composition, size, and shape [20, 21]. Ag and Au have gained research interest because of their strong resonance with ultraviolet (UV) and visible light. Moreover, the surface plasmon resonance (SPR) of metal NPs enhances the intensity of the electric field near the metal NPs, thereby significantly increasing the rate of electron–hole (e–h) pair generation [20, 22]. Plasmonic metal NPs also act as dye sensitizers by absorbing resonant photons and injecting high-energy electrons into the nearby semiconductor [20, 23]. Kang et al. reported the effective injection of SPR-excited electrons, i.e., hot electrons, by Au NPs into the conduction band of MoS₂ by overcoming the Schottky barrier (~0.8 eV) of Au/MoS₂ [24]. Plasmonic effect has been effectively applied to enhance the photocatalytic and PEC performances of various semiconductors, such as TiO₂, CdS, ZnO, and BiFeO₃ [25–32]. To maximize the SPR effects and enhance the PEC activity, SPR-induced charge carriers should be efficiently transported to the corresponding electrode/water interfaces. Vertically aligned few-layer MoS₂ nanosheets on graphene can act as desirable heterostructures to synergistically exploit the SPR effects in terms of energy band diagram and physical nanostructure architecture.

Herein, we report significantly improved PEC efficiency through the synergetic effects of (1) SPR-enhanced optical absorption and photo-generation of charge carriers and (2) efficient separation and transportation of photo-generated

e–h pairs through few-layer MoS₂ sheets that are vertically aligned on graphene. Few-layer MoS₂ sheets were vertically grown on graphene in a controlled manner at relatively low temperatures (250 °C) through metalorganic chemical vapor deposition (MOCVD) to minimize damage to the graphene. For the SPR effect, Ag NPs were formed on 2D MoS₂ sheets on graphene through simple thermal evaporation of Ag (Fig. 1). Thermal evaporation is a low-cost and practical method for large-area substrates in comparison with previously reported methods, such as sophisticated metal nanopatterning [21], drop/spin casting of pre-synthesized metal NPs [33], and chemical synthesis [22]. Ag was chosen as plasmonic metal because of its appropriate resonant wavelength range in the UV to near-infrared (IR) band and smaller work function (~4.3–4.8 eV) than Au (~5.1–5.5 eV) and Pt (~5.1–5.9 eV). Thus, Ag/MoS₂ forms a low Schottky barrier, which is advantageous for the efficient injection of SPR-excited electrons into the conduction band of MoS₂.

2 Experimental

2.1 Preparation of heterostructures of graphene/2D MoS₂/Ag NPs

Graphene was synthesized on Cu foils (Alfa Aesar) by using inductively coupled plasma (ICP) CVD with CH₄ and H₂ gases at 950 °C for 5 min. The ICP power and growth pressure were fixed at 200 W and 1 Torr, respectively. The synthesized graphene on Cu was transferred on an ITO glass substrate (Fig. 1). The CVD growth and transfer procedures of graphene were further described elsewhere [34]. MoS₂ was directly grown on ITO and ITO/graphene at 250 °C by using MOCVD with Mo(CO)₆ and

H₂S gas (5 vol% in balance N₂) as Mo and S precursors, respectively. Mo(CO)₆ was vaporized at 20 °C and transferred into a quartz reaction tube with Ar gas of 25 standard cubic centimeters per minute (SCCM). The flow rate of H₂S gas was 75 SCCM. The growth pressure and time were fixed at 1 Torr and 5 min, respectively. Ag NPs were formed on ITO/graphene/MoS₂ through thermal evaporation of Ag at room temperature. The size and coverage of Ag NPs on few-layer MoS₂ were controlled by various nominal Ag deposition thicknesses of 2, 4, and 8 nm. The Ag contents per electrode area were estimated to be 2.1, 4.2, and 8.4 μg cm⁻² for 2, 4, and 8 nm of Ag, respectively.

2.2 Characterization

The morphology of the samples was investigated via scanning electron microscopy (SEM; Hitachi S-4800) and transmission electron microscopy (TEM; Tecnai G² F30 S-Twin). The structural properties of MoS₂ were characterized by TEM and micro-Raman spectroscopy by using an excitation band of 532 nm and a charge-coupled device detector. The chemical states and composition of the samples were characterized by X-ray photoelectron spectroscopy (XPS; Thermo Fisher K-Alpha+). Optical properties were evaluated by UV–visible (UV–Vis; Scinco S-3100) and photoluminescence (PL) spectroscopy (excitation at 532 nm). Photoexcited carrier behavior was investigated by time-resolved PL (TRPL) measurements. The samples were excited using a 467 nm pulsed laser, and the transient signal was recorded using a time-correlated single-photon counting spectrometer (Horiba Fluorolog 3). The energy level of MoS₂ was evaluated via UV photoelectron spectroscopy (UPS; Thermo scientific, K-alpha⁺).

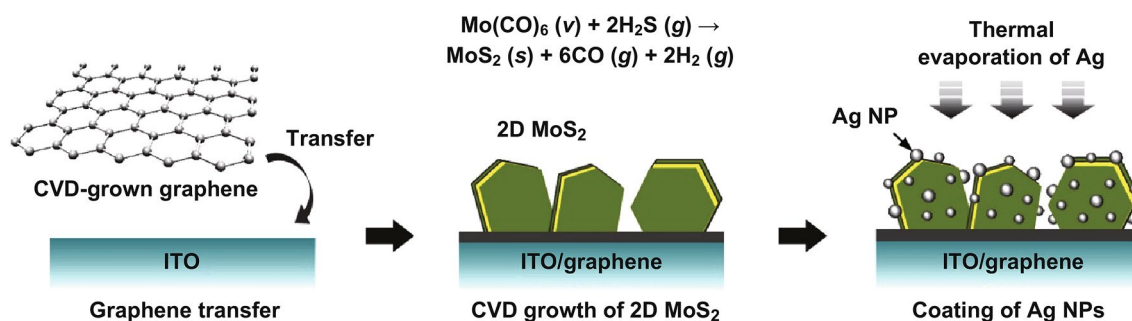


Fig. 1 Schematic of preparation of plasmonic Ag-decorated vertically aligned few-layer MoS₂ nanosheets on graphene

2.3 Photoelectrochemical Measurement

PEC cells were fabricated on $1 \times 2 \text{ cm}^2$ ITO glass substrates. The working area of the PEC cells was fixed at $0.5 \times 0.5 \text{ cm}^2$ by using non-conductive epoxy to cover the undesired areas. PEC characterization was performed using a three-electrode system and an electrochemical analyzer (potentiostat/galvanostat 263A). A Pt plate and KCl-saturated calomel ($\text{Hg}/\text{Hg}_2\text{Cl}_2$) were used as counter and reference electrodes, respectively. The electrolyte solutions were prepared with $0.3 \text{ M KH}_2\text{PO}_4 + 0.3 \text{ M KOH}$ and $0.5 \text{ M Na}_2\text{SO}_3 + 0.5 \text{ M Na}_2\text{SO}_4$. The light source was simulated AM 1.5G irradiation of 100 Mw cm^{-2} delivered by a 150 W Xe arc lamp. The current density–voltage characteristics were recorded using a source meter (Keithley 2400). Electrochemical impedance spectroscopy (EIS) measurement was performed under constant light illumination (100 mW cm^{-2}) at a bias of 0.6 V with varying AC frequencies from 100 kHz to 100 mHz . The incident monochromatic photon-to-current conversion efficiency (IPCE) of the electrode structure was measured using a grating monochromator in the excitation wavelength range of $300\text{--}800 \text{ nm}$. The hydrogen gas products were analyzed using a YL 6500 gas chromatograph (Young In Chromass Co., Ltd.) equipped with a flame ionization detector and a thermal conductivity detector. A gas volume of 0.5 mL

was injected into columns of 40/60 Carboxen-1000 for GC analysis.

3 Results and Discussion

3.1 Microstructure of AgNP-Decorated MoS_2 Nanosheets on Graphene

MoS_2 nanosheets with a height of $\sim 200 \text{ nm}$ and length of $\sim 150\text{--}250 \text{ nm}$ were vertically aligned and densely packed on the ITO/graphene substrate (hereinafter referred to as G/MoS_2 , Fig. 2a, b). Owing to the low-temperature growth at $250 \text{ }^\circ\text{C}$, the graphene layer remained after the MOCVD growth of MoS_2 , as confirmed by the presence of the characteristic G and 2D band peaks in the Raman spectrum (inset of Fig. 2a, Fig. S1a, b). The pristine CVD-grown graphene layer exhibited a low-intensity ratio of D to G band peaks (> 0.15) and an excellent light transmittance of 96.8% at 550 nm (Fig. S1c), corresponding to approximately one and a half layers of high-quality graphene [34]. The structure of few-layer MoS_2 was investigated using TEM and Raman spectroscopy. The planar-view TEM image of G/MoS_2 clearly showed the layered structure of MoS_2 sheets with edges on graphene (Fig. 2c). The sheets comprised 1–5 layers with an interlayer spacing of 0.63 nm , corresponding to the semiconducting 2H MoS_2 .

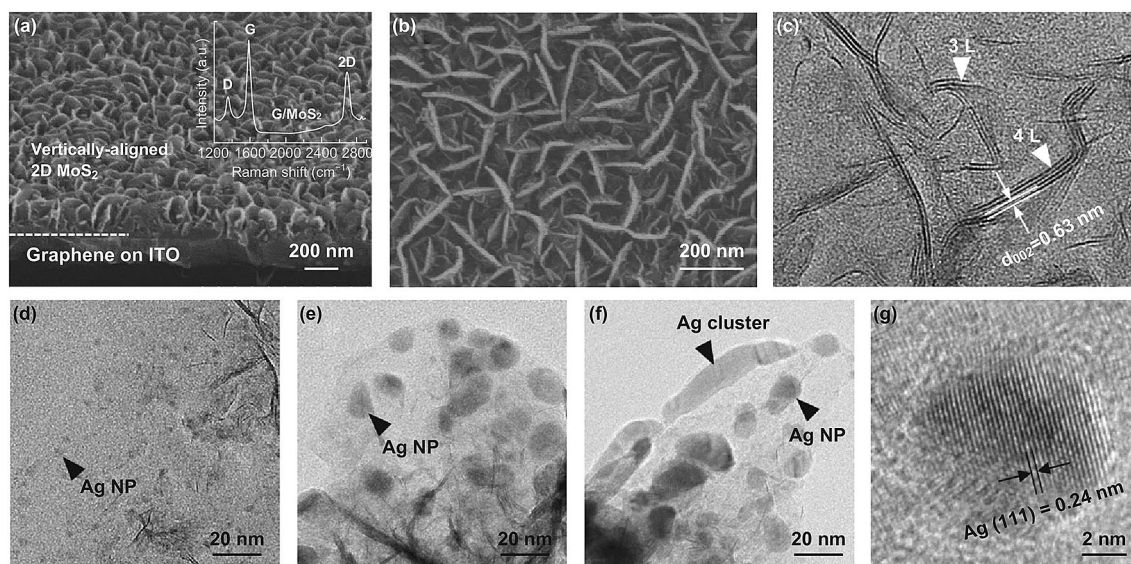


Fig. 2 **a** Tilted-view SEM, **b** planar-view SEM, and **c** planar-view TEM images of vertically aligned MoS_2 nanosheets on graphene (G/MoS_2). The inset in **a** is the Raman spectrum of G/MoS_2 . TEM images of Ag-decorated vertically aligned few-layer MoS_2 nanosheets on graphene: **d** $\text{G}/\text{MoS}_2/\text{Ag}$ -2, **e** $\text{G}/\text{MoS}_2/\text{Ag}$ -4, and **f** $\text{G}/\text{MoS}_2/\text{Ag}$ -8. **g** High-resolution lattice TEM image of an Ag NP in $\text{G}/\text{MoS}_2/\text{Ag}$ -4

The TEM results are consistent with the Raman spectrum of G/MoS₂ (Fig. S2a). The E_{2g}^1 and A_{1g} modes can be attributed to the in-plane vibration of Mo and S atoms and the out-of-plane vibration of S atoms, respectively. The positions and relative frequency difference (RFD) of E_{2g}^1 and the A_{1g} peaks are strongly correlated with the number of MoS₂ layers [12, 35, 36]. For G/MoS₂, the RFD value (22.3 cm^{-1}) of E_{2g}^1 (385.0 cm^{-1}) and A_{1g} peaks (407.3 cm^{-1}) corresponds to a few layers of MoS₂. The MoS₂ sheets grown on ITO (hereinafter referred to as ITO/MoS₂) showed similar size and morphology as the counterpart sample, namely G/MoS₂ (Fig. S2b). The RED value of E_{2g}^1 and A_{1g} peaks of ITO/MoS₂ was also similar to that of G/MoS₂ (Fig. S2a).

Figure 2d–f shows the TEM images of Ag-decorated G/MoS₂ with nominal Ag thicknesses of 2, 4, and 8 nm, respectively (referred to as G/MoS₂/Ag-2, G/MoS₂/Ag-4, and G/MoS₂/Ag-8, respectively). The size of the Ag NPs on MoS₂ was successfully manipulated by varying the nominal deposition thickness of Ag through thermal evaporation. For G/MoS₂/Ag-2, Ag NPs with a size of ~3–5 nm were formed on the MoS₂ nanosheet surface (Fig. S3). The NP size increased to ~10–20 nm for G/MoS₂/Ag-4. By increasing the nominal deposition thickness to 8 nm, the size of Ag NPs increased to ~20–40 nm. In addition, large Ag clusters of ~60–100 nm were partially formed. The high-resolution TEM lattice image revealed that the NPs were metallic Ag (Fig. 2g). The metallic Ag was also confirmed by XPS. Figure 3a shows two strong peaks in the XPS spectrum of G/MoS₂/Ag-4 at 373.9 and 367.9 eV, which can be attributed to the Ag $3d_{3/2}$ and Ag $3d_{5/2}$ orbitals of metallic Ag, respectively [37].

MoS₂ presents two common structure polymorphs, namely semiconducting 2H and metallic 1T phases, which can be converted from each other by surface treatments, such as Ar-plasma bombardment and metal deposition [2, 38, 39]. As shown in Fig. 3b, the XPS spectra of the Mo $3d$ core level were deconvoluted into only two peaks at 229.1 and 232.2 eV, which can be attributed to the Mo⁴⁺ $3d_{5/2}$ and Mo⁴⁺ $3d_{3/2}$ components of the 2H phase of MoS₂, respectively [2, 38, 39]. Pristine MoS₂ (G/MoS₂) and Ag NP-decorated MoS₂ (G/MoS₂/Ag-4) exhibited nearly identical XPS spectra at the Mo $3d$ core level, indicating that the single phase of semiconducting 2H MoS₂ remained stable after Ag NP decoration. This structural stability is highly advantageous for 2D MoS₂ in semiconducting photoelectrode applications. Figure 3c shows the XPS spectra of the S $2p$ core level of MoS₂. The spectra were deconvoluted into two peaks at 163.2 and 162.0 eV, corresponding to the S $2p_{1/2}$ and S $2p_{3/2}$ orbital of divalent sulfur, respectively [38]. The ratios of the S $2p_{1/2}$ and S $2p_{3/2}$ peaks of G/MoS₂ and G/MoS₂/Ag-4 were almost identical, suggesting a single phase of 2H MoS₂ for both samples. The 2H phase of both samples was also confirmed by TEM (Fig. 2c). G/MoS₂/Ag-4 exhibited a small broad bump near 168 eV, which can be attributed to S⁴⁺ due to Ag sulfurization. However, the peak was removed by slight Ar-plasma surface etching, indicating the ultrathin layer of silver sulfide. The XPS result implies that the interface of MoS₂/Ag is likely to be an alloy interface.

3.2 Effect of Graphene on the PEC Activity of MoS₂ Nanosheets

The G/MoS₂ and ITO/MoS₂ samples exhibited a PL peak at 676 nm (inset of Fig. 4a), which is consistent with the

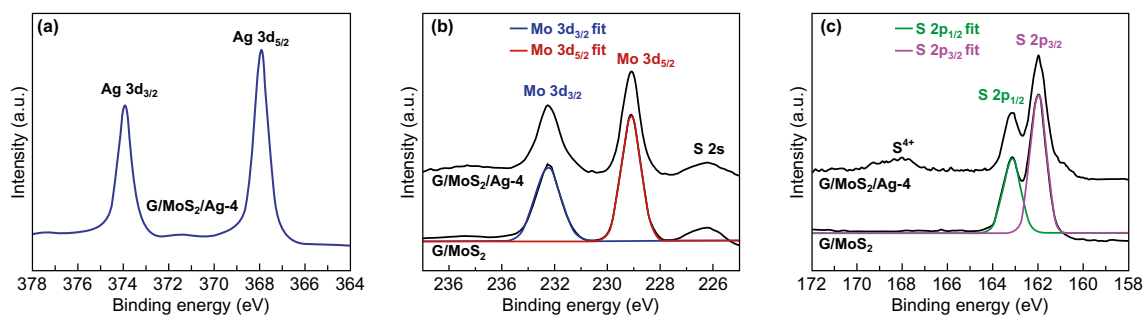


Fig. 3 XPS spectra of **a** Ag $3d$, **b** Mo $3d$, and **c** S $2p$ core levels in G/MoS₂ and G/MoS₂/Ag-4

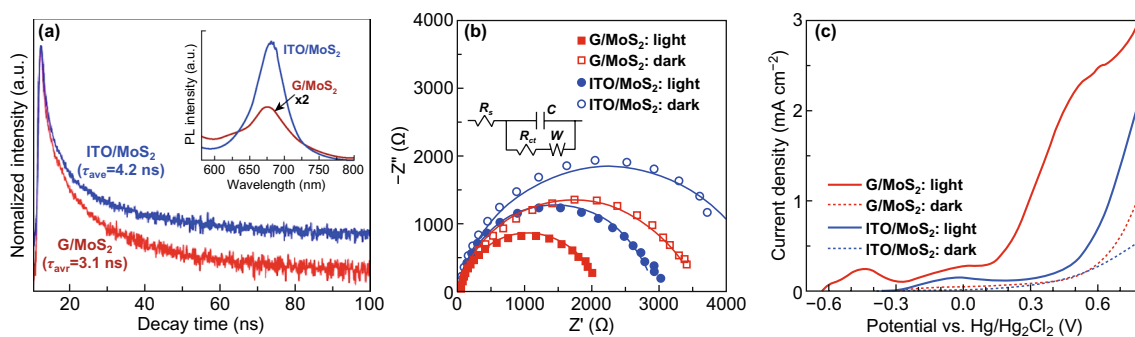


Fig. 4 **a** TRPL results of ITO/MoS₂ and G/MoS₂. The inset shows the corresponding PL spectra. **b** Nyquist plots of ITO/MoS₂ and G/MoS₂ in the dark and under illumination. The inset shows the equivalent Randles circuit. **c** Photo- and dark current densities versus the potential curves of PEC cells with working electrodes of ITO/MoS₂ and G/MoS₂

energy of exciton A. Hence, the dominant electronic transition was the direct bandgap transitions at the *K* point [12]. Notably, G/MoS₂ achieved significantly lower PL efficiencies than ITO/MoS₂. The PL quenching efficiency indicated that the graphene layer played a crucial role in reducing the e–h recombination in MoS₂. TRPL spectroscopy study was conducted to further understand the dynamic behavior of photo-generated carriers (Fig. 4a). The average carrier lifetimes were extracted using the PL decay kinetics fitted by a bi-exponential decay profile [40]. G/MoS₂ exhibited a shorter carrier lifetime of 3.1 ns than ITO/MoS₂ (4.2 ns). The reduced carrier lifetime can be attributed to the benefits of graphene/MoS₂ heterojunction for efficient separation and transportation of photo-generated carriers to the semiconductor/liquid interface [18].

EIS study was conducted to further understand the charge transport property. Figure 4b shows the Nyquist plots of EIS in the dark and under illumination. G/MoS₂ exhibited smaller EIS semicircles than ITO/MoS₂, whose radius mirrors the charge transfer resistance (R_{ct}). The Nyquist plots were fitted using a simplified Randles circuit (inset of Fig. 4b), consisting of R_{ct} , solution resistance (R_s), constant phase element (Q), and diffusion of species in electrolyte solution represented by Warburg impedance (W). The R_{ct} values are listed in Supporting Information (Table S1). G/MoS₂ had R_{ct} values of 3264 and 1959 Ω , whereas ITO/MoS₂ exhibited R_{ct} values of 4236 and 2766 Ω in the dark and under illumination, respectively. Moreover, the R_{ct} (dark)-to- R_{ct} (photo) ratio (1.67) of G/MoS₂ was greater than that of ITO/MoS₂ (1.53), suggesting that the photo-generated e–h pairs were efficiently separated and transported through the graphene/MoS₂ heterojunction.

Considering the benefits of graphene/MoS₂ heterojunction, G/MoS₂ exhibited significantly higher PEC activity through the measured potential range than ITO/MoS₂ (Fig. 4c). G/MoS₂ yielded approximately nine times higher photocurrent density (1.72 mA cm⁻²) at 0.4 V (at which the photo-to-dark current ratio (I_{ph}/I_{dark}) was at maximum) than ITO/MoS₂ (0.19 mA cm⁻²). The maximum I_{ph}/I_{dark} value of G/MoS₂ was approximately 16 at 0.4 V, whereas that of ITO/MoS₂ was approximately 4 at 0.8 V. The water oxidation onset potential (~ 0.13 V), which is generally defined by the potential at the intersection of the dark current and the tangent at the maximum slope of the photocurrent, of G/MoS₂ had a cathodic shift of ~ 0.41 V with respect to that (~ 0.54 V) of ITO/MoS₂. The rapidly increasing photocurrent density of the samples above 0.6 V resulted from the considerably high dark current, which can be attributed to the electrocatalysis and electro-corrosion of MoS₂, in which active S atoms can react with redox species in the solution [12, 14].

3.3 Effect of Plasmonic Ag NPs on the PEC Activity of Graphene/MoS₂ Nanosheets

Raman spectroscopy characterization was performed to investigate the interaction of Ag NPs with MoS₂. The characteristic E_{2g}^1 and A_{1g} modes of the Ag-decorated samples were redshifted with respect to those of G/MoS₂-250 because of the stiffening of E_{2g}^1 and A_{1g} vibrations (Fig. 5a). The stiffened lateral vibration between Mo and S atoms through E_{2g}^1 mode resulted from the p-doping effect of Ag NPs in MoS₂ [38]. MoS₂/Ag was very likely to form a

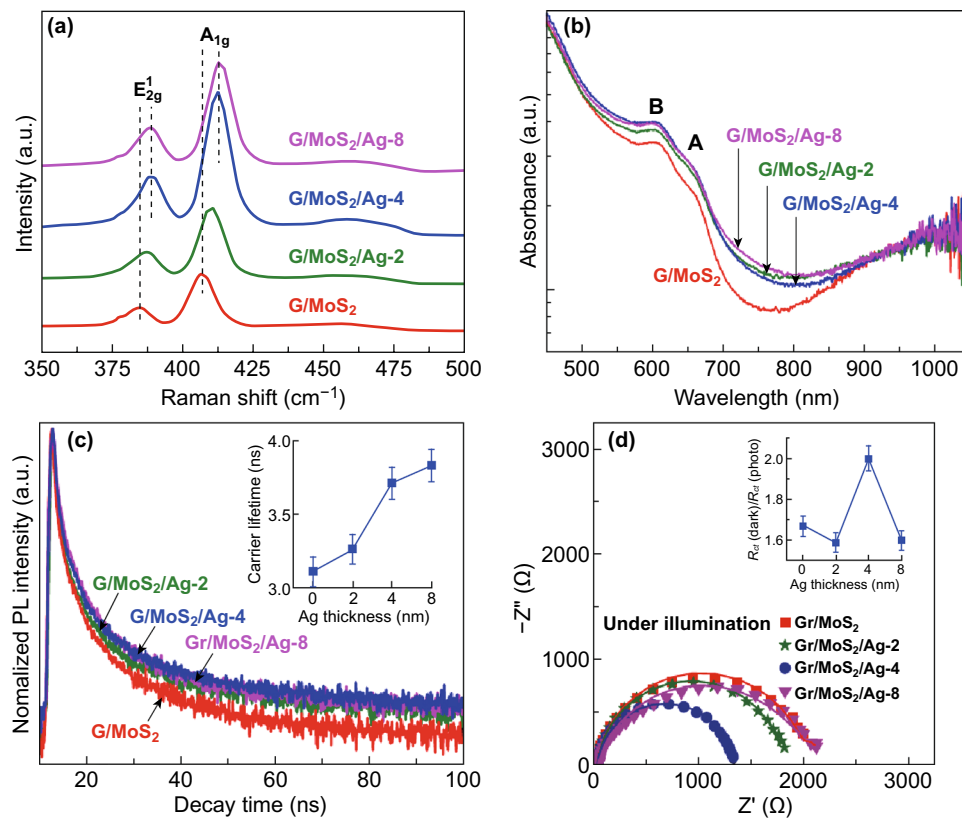


Fig. 5 **a** Raman spectra, **b** UV-Vis absorption, **c** TRPL results, and **d** Nyquist plots of G/MoS₂, G/MoS₂/Ag-2, G/MoS₂/Ag-4, and G/MoS₂/Ag-8. The inset in **c** shows the carrier lifetimes based on the corresponding TRPL measurements. The inset in **d** shows the R_{ct} (dark)/ R_{ct} (photo) values of G/MoS₂, G/MoS₂/Ag-2, G/MoS₂/Ag-4, and G/MoS₂/Ag-8

Schottky junction because of electron transfer from MoS₂ to Ag NPs, as shown in Fig. S4. The stiffened vertical vibration of S atoms through A_{1g} mode was also attributed to the interaction between the Ag NPs and MoS₂ [23]. Figure 5b shows the UV-Vis absorption spectra of G/MoS₂ and the Ag-decorated MoS₂ samples. All samples showed two prominent absorption peaks at approximately 607 and 663 nm. The two peaks, known as excitons B and A, respectively, can be attributed to the direct excitonic transitions at the K point of the MoS₂ Brillouin zone [12, 41]. In comparison with G/MoS₂, the Ag-decorated MoS₂ samples exhibited stronger absorption intensity, especially for red light and near-IR regions. Additionally, the absorption edges (~800 nm) of Ag-decorated MoS₂ samples were redshifted with respect to that (~750 nm) of G/MoS₂. The enhanced visible light and broadened absorption near the IR region can be attributed to the strong coupling between the excitons and surface plasmons of Ag NPs [20, 21]. The PL spectra also exhibited redshifting behavior with increasing Ag NP sizes (Fig. S5).

G/MoS₂ showed a PL peak position of 676 nm, corresponding to the energy of the exciton A, representing the direct bandgap transitions at the K point of 2D MoS₂. With increasing Ag NP sizes, the PL peak was gradually redshifted, reaching 688 nm for G/MoS₂/Ag-8.

TRPL study was conducted to investigate the plasmonic effect of Ag NPs on the dynamic carrier behavior. G/MoS₂ exhibited the shortest carrier lifetime of 3.1 ns, whereas G/MoS₂/Ag-4 and G/MoS₂/Ag-8 yielded longer carrier lifetimes of ~3.8 ns (Fig. 5c). The carrier lifetime increased with increasing nominal Ag deposition thicknesses. The long carrier lifetimes of Ag-decorated MoS₂ samples can be attributed to suppressed e-h recombination by filling the trapping sites of MoS₂ by plasmon-excited electrons [23]. Ag-decorated MoS₂ samples also exhibited smaller EIS semicircles than G/MoS₂ (Fig. 5d, Fig. S5). The Nyquist plots of G/MoS₂/Ag-4 yielded the lowest R_{ct} in the dark (~2572 Ω) and under illumination (~1284 Ω), suggesting the effective assistance of the carrier transfer through the Ag

NPs on the MoS₂ surface. Moreover, G/MoS₂/Ag-4 yielded the highest R_{ct} (dark)/ R_{ct} (photo) of 2.00 (inset of Fig. 5d). The increased R_{ct} (dark)/ R_{ct} (photo) can result from the SPR-enhanced photo-generation and transfer rate of the charge carriers. In addition, the heterojunction of MoS₂/Ag can play a significant role in improving the charge separation and transfer rate [42, 43].

To validate the experimental findings, finite-difference time-domain (FDTD) simulations of the interaction of materials with the incident electromagnetic radiation were performed based on Maxwell's equations. Ag hemispheres in an open-air environment under the illumination of a plane-wave source were considered (Fig. S7). A 2D periodic orientation of the NPs on a three-layer-thick MoS₂ substrate was assumed including the following: (1) 3-nm-diameter NPs with a pitch of 20 nm (referred to as AgNP-3), (2) 15-nm-diameter NPs with a pitch of 30 nm (referred to as AgNP-15), and (3) 60-nm-diameter NPs with a pitch of 65 nm (referred to as AgNP-60). The electric field vector of the source oscillated along the x -axis, while the propagation vector is along the z -axis. Figure 6 shows the simulated

UV–Vis absorption spectra and electric field distribution contour plots at the wavelength of SPR (λ_{SPR}) for AgNP-3, AgNP-15, and AgNP-60. The simulated UV–Vis absorption spectrum of pristine MoS₂ substrate was in good agreement with the corresponding experimental result (Fig. 6a). The light absorption was significantly enhanced in the visible light and IR regions by Ag NP decoration. Notably, the SPR peaks appeared above the absorption edge of pristine MoS₂ (~ 700 nm), consistent with the experimentally observed broadened absorption near the IR region. AgNP-15 exhibited the strongest SPR effect, resulting in the highly amplified local electric field intensity in MoS₂ (Fig. 6b). The SPR-enhanced electric field can increase the rate of e–h pair generation by a few orders of magnitude [20]. The 15 nm Ag NPs induced an SPR-enhanced electric field in the entire interface region of MoS₂/Ag NP. By contrast, the 60 nm Ag NPs showed SPR effect only along the edge of NPs (Fig. 6c), indicating that a significant amount of light was extinguished by big Ag clusters (~ 60 – 100 nm) of G/MoS₂/Ag-8 without photo-generation of e–h pairs in MoS₂. The excessive surface coverage of metal NPs can also hinder contact of the

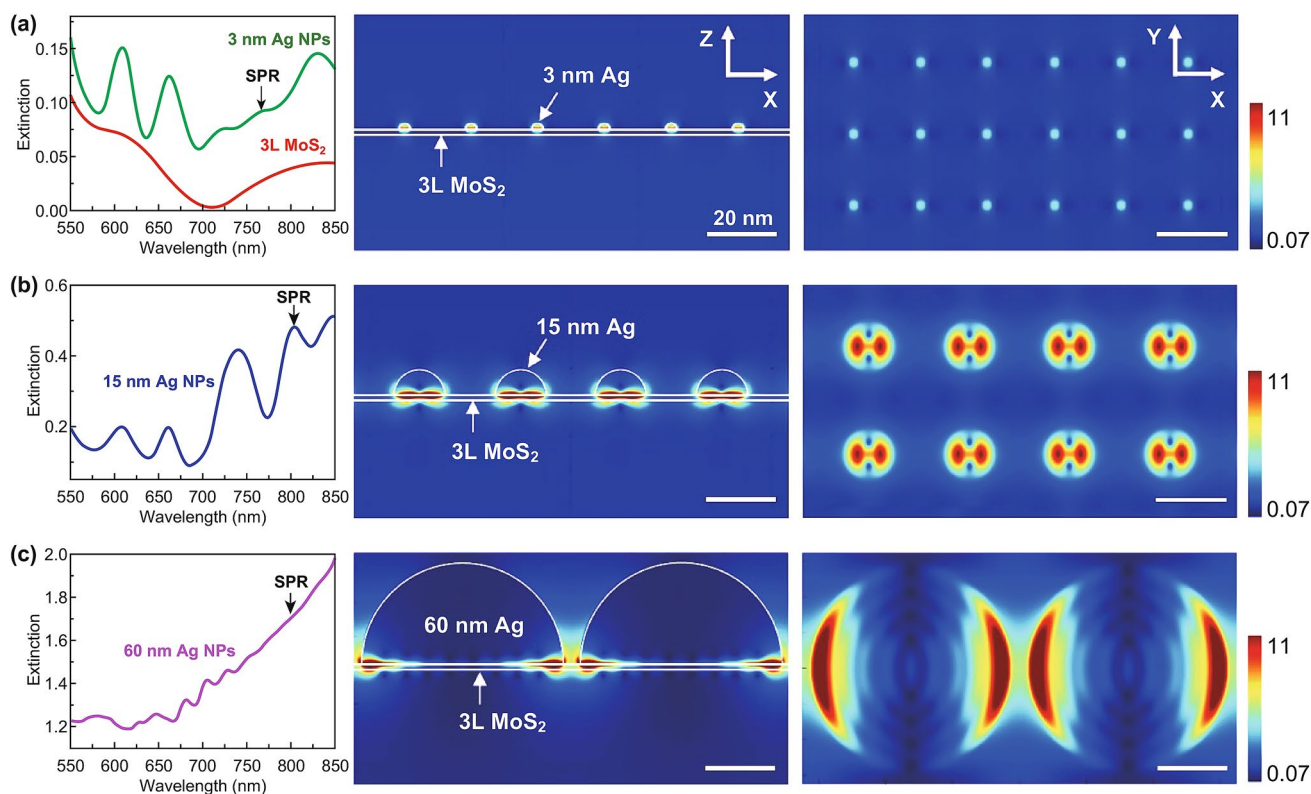


Fig. 6 Simulated UV–Vis absorption spectra and electric field distribution contour plots at λ_{SPR} for **a** AgNP-3, **b** AgNP-15, and **c** AgNP-60

electrochemical active surface with the electrolyte solution, resulting in deteriorated PEC activity [44, 45]. In addition, the surface plasmons of small Ag NPs (< 30 nm) undergo decay because of the formation of energetic charge carriers, but those of large Ag NPs (> 50 nm) undergo decay through the radiative scattering of resonant photons [37, 46]. Thus, the Ag NPs of G/MoS₂/Ag-4 efficiently injected SPR-excited electrons into the conduction band of MoS₂, resulting in the largest R_{ct} (dark)/ R_{ct} (photo). Meanwhile, the SPR effect of G/MoS₂/Ag-2 was relatively weak because of its low surface coverage of tiny Ag NPs of less than 10 nm (Fig. 6a).

To gain insight into the carrier transport property across the heterojunction of graphene/MoS₂, its electronic structure was studied by UPS. The work function of MoS₂ (4.82 ± 0.15 eV) was determined based on the difference between the photon energy of excited radiation (21.2 eV) and the spectrum width which is measured from the valence band and secondary edges (16.38 eV, Fig. 7a). The energy difference between the Fermi energy and valence band edge ($E_F - E_{VB}$) was 1.36 eV (Fig. 7b). Considering the band-gap energy of ~ 1.88 eV for MoS₂ based on the UV-Vis

absorption and PL spectra, the electron affinity of MoS₂ was approximately 4.33 eV, which is consistent with the previously reported values (~ 4.3 eV) [47]. This electronic structure suggests the n-type behavior of MoS₂, working as a photoanode. As shown in Fig. 7c, the Fermi level (~ 4.6 – 4.8 eV of work function) of pristine few-layer graphene [48] was appropriately located between the Fermi level of the ITO and the conduction band edge of MoS₂ for efficient extraction of electrons to the cathode.

Figure 8a shows the linear sweep voltammograms of G/MoS₂, G/MoS₂/Ag-2, G/MoS₂/Ag-4, and G/MoS₂/Ag-8 under illumination. The Ag-decorated MoS₂ samples exhibited significantly higher PEC activities than G/MoS₂, whereas the dark currents were almost identical (Fig. S8). Subsequently, G/MoS₂/Ag-4 yielded 2.5 times higher I_{ph}/I_{dark} value than G/MoS₂. In addition, the Ag-decorated MoS₂ samples showed a significant cathodic shift of onset potential up to 0.2 V with respect to that of G/MoS₂. The Ag-decorated MoS₂ samples also did not exhibit any anodic peaks before the onset potential, whereas G/MoS₂ yielded minor but noticeable peaks. The anodic peaks can

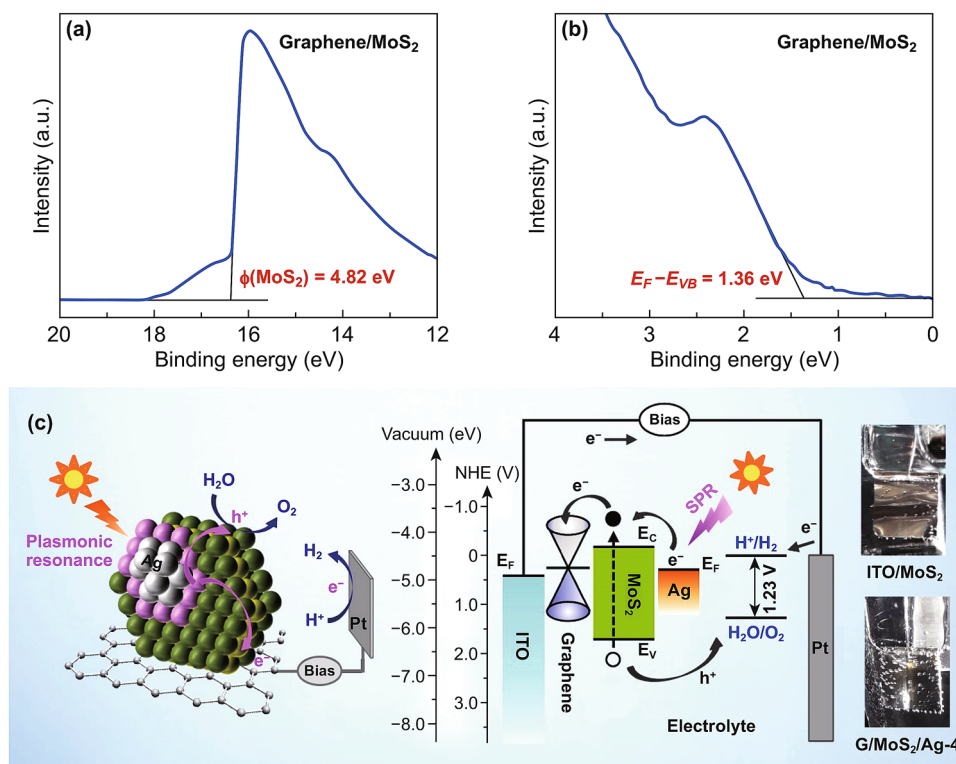


Fig. 7 **a** UPS secondary electron cutoff and **b** valence spectra of G/MoS₂. **c** PEC water-splitting working principle of plasmonic Ag-decorated vertically aligned few-layer MoS₂ nanosheets on graphene. The photographs in **c** show gas bubbling on the dark cathodes (Pt) for ITO/MoS₂ and G/MoS₂/Ag-4 during PEC measurement

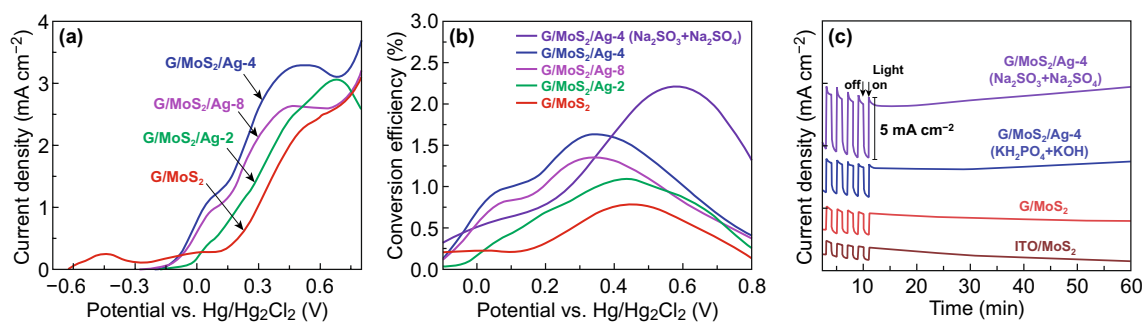


Fig. 8 **a** Photocurrent density–potential curves of PEC cells with various working electrodes (G/MoS₂, G/MoS₂/Ag-2, G/MoS₂/Ag-4, and G/MoS₂/Ag-8) in 0.3 M KH₂PO₄ + 0.3 M KOH solution. **b** Photoconversion efficiencies and **c** photocurrent–time plots for G/MoS₂, G/MoS₂/Ag-2, G/MoS₂/Ag-4, and G/MoS₂/Ag-8 in 0.3 M KH₂PO₄ + 0.3 M KOH solution and G/MoS₂/Ag-4 in 0.5 M Na₂SO₃ + 0.5 M Na₂SO₄ solution

be originated from surface states of 2D MoS₂ nanosheets, which can be filled and deactivated by plasmon-excited electrons [23]. Passivating surface states also caused the significant cathodic shift of onset potential [49] and prolonged the carrier lifetimes of the Ag-decorated MoS₂ samples (Fig. 5c). Photoconversion efficiency (η) was estimated using the following equation to further quantify PEC performance [50]:

$$\eta = J(E^{\circ} - V_{\text{app}}) / P_{\text{light}} \quad (1)$$

where J is the photocurrent density (mA cm^{-2}) at the applied potential, E° is the standard reversible potential (1.23 V), V_{app} is applied potential, and P_{light} is the power density of illumination. The photoconversion efficiencies of Ag-decorated MoS₂ samples were significantly higher than that (0.8% at -0.45 V) of G/MoS₂ (Fig. 8b). Among the samples, G/MoS₂/Ag-4 exhibited the highest photoconversion efficiency of 1.6% at -0.35 V. The photoconversion efficiency of G/MoS₂/Ag-4 further increased to 2.2% at -0.58 V in 0.5 M Na₂SO₃ + 0.5 M Na₂SO₄. The photoconversion efficiency G/MoS₂/Ag-4 was comparable with those of previously reported photoanodes, such as Au-decorated MoS₂ flakes on carbon fiber cloth (1.27%) [51], MoS₂ nanosheets on TiO₂ nanorods (0.81%) [52], Ag-embedded MoS₂/BiVO₄ heterojunctions (2.67%) [53], and MoS₂ nanosheets on polydopamine-modified TiO₂ nanotubes (1.56%) [54]. Moreover, the photocurrents of G/MoS₂ and G/MoS₂/Ag-4 did not change significantly after 1 h of illumination, whereas the photocurrent of ITO/MoS₂ decreased continuously (Fig. 8c). The photocurrents of G/MoS₂ and G/MoS₂/Ag-4 decayed initially but saturated shortly above 300 s. The decayed photocurrent was attributed to the recombination of the photo-generated holes with electrons [55]. The photocurrent became stable as the transfer and generation of

photo-generated e–h pairs reached equilibrium. The stable photocurrent suggests the effective separation and transfer of the photo-generated e–h pairs in the heterojunction of graphene/MoS₂ nanosheets. To examine the PEC stability of Ag-decorated MoS₂, the time-dependent PEC measurement of the G/MoS₂/Ag-4 was repeated after a month. The time-dependent behavior did not change significantly excepting for slightly reduced photocurrents (Fig. S9). After PEC measurement for 1 h, the MoS₂ nanosheets on ITO (ITO/MoS₂) were significantly damaged, whereas G/MoS₂ and G/MoS₂/Ag-4 showed slight morphological changes (Fig. S10). We recently reported that such morphological changes in MoS₂ nanosheets were due to the decomposition of MoS₂, mainly the loss of S elements [12].

IPCE and H₂ evolution studies were carried out to gain insights into the enhanced PEC performance by G/MoS₂ heterojunction and SPR effects. Figure 9a shows the IPCE plots of various working electrodes (MoS₂, G/MoS₂, and G/MoS₂/Ag-4). G/MoS₂/Ag-4 exhibited significantly improved photoconversion efficiencies over the overall incident-light waveband, suggesting fortified carrier photo-generation and transfer dynamics. Furthermore, a significant IPCE enhancement was observed at the ~ 650 – 750 nm region, which was associated with the SPR effect of Ag NPs. Hydrogen evolution from dark cathode (Pt) was measured at 0.6 V versus Hg/Hg₂Cl₂ by using a three-electrode configuration during 15 min. The amount of H₂ produced was significantly increased by G/MoS₂ heterojunction and SPR effects, suggesting that the photocurrent was attributed to the water-splitting reaction. In addition, the Faradaic efficiency of G/MoS₂/Ag-4 was estimated to be approximately 90.4%, implying that few side reactions occurred during water splitting [56].

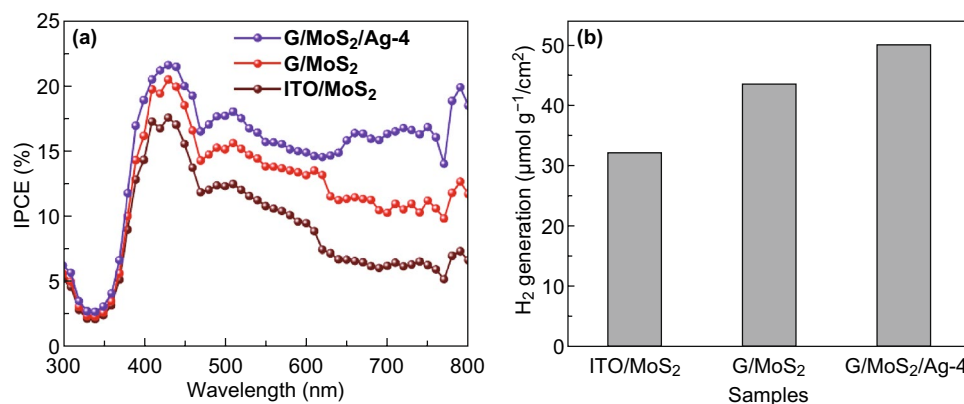


Fig. 9 **a** IPCE plots and **b** hydrogen evolution amounts for 15 min of PEC cells with various working electrodes (ITO/MoS₂, G/MoS₂, and G/MoS₂/Ag-4) in 0.5 M Na₂SO₃ + 0.5 M Na₂SO₄ solution

4 Conclusion

Plasmonic Ag-decorated vertically aligned few-layer MoS₂ nanosheets were prepared on graphene in a practical manner through MOCVD of MoS₂ and thermal evaporation of Ag. G/MoS₂ showed up to four times higher I_{ph}/I_{dark} than ITO/MoS₂ because of the efficient separation and transportation of the photo-generated carriers by the graphene/2D MoS₂ heterojunction. The PEC activity of G/MoS₂ was further enhanced by plasmonic Ag NP decoration. G/MoS₂/Ag-4 yielded 10 times higher I_{ph}/I_{dark} value than ITO/MoS₂. The maximum photoconversion efficiency of G/MoS₂/Ag-4 was 2.2% at -0.58 V. The significantly improved PEC performance was attributed to the synergistic effects of SPR and graphene/2D MoS₂ heterojunction. Plasmonic Ag NPs enhanced visible-light and near-IR absorption of 2D MoS₂, resulting in significantly increased the photo-generation rate of e⁻-h⁺ pairs. Subsequently, the e⁻-h⁺ pairs were efficiently separated and transported to catalytic surfaces across the favorable graphene/2D MoS₂ heterojunction and along the highly conductive edges of the vertically aligned 2D MoS₂, thereby significantly enhancing the PEC activity. This study offers a practical large-scale approach that combines the potential of SPR and graphene/2D MoS₂ heterojunction effects for efficient PEC applications.

Acknowledgements This work was supported by the National Research Foundation of Korea (NRF) grants funded by the Ministry of Education (2020R111A3A04037241 and 2019R1A6A3A13095792) and the Korea Government (MSIT) (2020R1A4A4079397).

Open Access This article is licensed under a Creative Commons Attribution 4.0 International License, which permits use, sharing, adaptation, distribution and reproduction in any medium or format, as long as you give appropriate credit to the original author(s) and the source, provide a link to the Creative Commons licence, and indicate if changes were made. The images or other third party material in this article are included in the article's Creative Commons licence, unless indicated otherwise in a credit line to the material. If material is not included in the article's Creative Commons licence and your intended use is not permitted by statutory regulation or exceeds the permitted use, you will need to obtain permission directly from the copyright holder. To view a copy of this licence, visit <http://creativecommons.org/licenses/by/4.0/>.

Electronic supplementary material The online version of this article (<https://doi.org/10.1007/s40820-020-00512-3>) contains supplementary material, which is available to authorized users.

References

1. M.G. Walter, E.L. Warren, J.R. McKone, S.W. Boettcher, Q. Mi, E.A. Santori, N.S. Lewis, Solar water splitting cells. *Chem. Rev.* **110**(11), 6446–6473 (2010). <https://doi.org/10.1021/cr1002326>
2. Q. Ding, B. Song, P. Xu, S. Jin, Efficient electrocatalytic and photoelectrochemical hydrogen generation using MoS₂ and related compounds. *Chem* **1**(5), 699–726 (2016). <https://doi.org/10.1016/j.chempr.2016.10.007>
3. B. Han, Y.H. Hu, MoS₂ as a co-catalyst for photocatalytic hydrogen production from water. *Energy Sci. Eng.* **4**(5), 285–304 (2016). <https://doi.org/10.1002/ese3.128>
4. B. Chen, Y. Meng, J. Sha, C. Zhong, W. Hu, N. Zhao, Preparation of MoS₂/TiO₂ based nanocomposites for photocatalysis and rechargeable batteries: progress, challenges, and perspective. *Nanoscale* **10**(1), 34–68 (2018). <https://doi.org/10.1039/C7NR07366F>

5. Y.H. Chiu, T.F.M. Chang, C.Y. Chen, M. Sone, Y.J. Hsu, Mechanistic insights into photodegradation of organic dyes using heterostructure photocatalysts. *Catalysts* **9**(5), 430 (2019). <https://doi.org/10.3390/catal9050430>
6. Y.H. Chiu, T.H. Lai, M.Y. Kuo, P.Y. Hsieh, Y.J. Hsu, Photoelectrochemical cells for solar hydrogen production: challenges and opportunities. *APL Mater.* **7**(8), 080901 (2019). <https://doi.org/10.1063/1.5109785>
7. M.J. Fang, C.W. Tsao, Y.J. Hsu, Semiconductor nanoheterostructures for photoconversion applications. *J. Phys. D Appl. Phys.* **53**(14), 143001 (2020). <https://doi.org/10.1088/1361-6463/ab5f25>
8. H. Li, Q. Zhang, C.C.R. Yap, B.K. Tay, T.H.T. Edwin, A. Olivier, D. Baillargeat, From bulk to monolayer MoS₂: evolution of raman scattering. *Adv. Funct. Mater.* **22**(7), 1385–1390 (2012). <https://doi.org/10.1002/adfm.201102111>
9. K.F. Mak, C. Lee, J. Hone, J. Shan, T.F. Heinz, Atomically thin MoS₂: a new direct-gap semiconductor. *Phys. Rev. Lett.* **105**(13), 136805 (2010). <https://doi.org/10.1103/PhysRevLett.105.136805>
10. C. Lee, H. Yan, L.E. Brus, T.F. Heinz, J. Hone, S. Ryu, Anomalous lattice vibrations of single- and few-layer MoS₂. *ACS Nano* **4**(5), 2695–2700 (2010). <https://doi.org/10.1021/nn1003937>
11. H. He, J. Lin, W. Fu, X. Wang, H. Wang et al., MoS₂/TiO₂ edge-on heterostructure for efficient photocatalytic hydrogen evolution. *Adv. Energy Mater.* **6**(14), 1600464 (2016). <https://doi.org/10.1002/aenm.201600464>
12. T.N. Trung, D.B. Seo, N.D. Quang, D. Kim, E.T. Kim, Enhanced photoelectrochemical activity in the heterostructure of vertically aligned few-layer MoS₂ flakes on ZnO. *Electrochim. Acta* **260**, 150–156 (2018). <https://doi.org/10.1016/j.electacta.2017.11.089>
13. D.B. Seo, S. Kim, T.N. Trung, D. Kim, E.T. Kim, Conformal growth of few-layer MoS₂ flakes on closely-packed TiO₂ nanowires and their enhanced photoelectrochemical reactivity. *J. Alloys Compd.* **770**, 686–691 (2019). <https://doi.org/10.1016/j.jallcom.2018.08.151>
14. K. Chang, Z. Mei, T. Wang, Q. Kang, S. Ouyang, J. Ye, MoS₂/graphene cocatalyst for efficient photocatalytic H₂ evolution under visible light irradiation. *ACS Nano* **8**(7), 7078–7087 (2014). <https://doi.org/10.1021/nn5019945>
15. F. Carraro, L. Calvillo, M. Cattelan, M. Favaro, M. Righetto et al., Fast one-pot synthesis of MoS₂/crumpled graphene p–n nanojunctions for enhanced photoelectrochemical hydrogen production. *ACS Appl. Mater. Interfaces* **7**(46), 25685–25692 (2015). <https://doi.org/10.1021/acsami.5b06668>
16. R.K. Biroju, D. Das, R. Sharma, S. Pal, L.P.L. Mawlong et al., Hydrogen evolution reaction activity of graphene–MoS₂ van der waals heterostructures. *ACS Energy Lett.* **2**(6), 1355–1361 (2017). <https://doi.org/10.1021/acsenenergylett.7b00349>
17. Z. Huang, W. Han, H. Tang, L. Ren, D.S. Chander, X. Qi, H. Zhang, Photoelectrochemical-type sunlight photodetector based on MoS₂/graphene heterostructure. *2D Mater.* **2**(3), 035011 (2015). <https://doi.org/10.1088/2053-1583/2/3/035011>
18. X. Yu, R. Du, B. Li, Y. Zhanga, H. Liu, J. Qu, X. An, Biomolecule-assisted self-assembly of CdS/MoS₂/graphene hollow spheres as high-efficiency photocatalysts for hydrogen evolution without noble metals. *Appl. Catal. B* **182**, 504–512 (2016). <https://doi.org/10.1016/j.apcatb.2015.09.003>
19. W. Zhou, K. Zhou, D. Hou, X. Liu, G. Li et al., Three-dimensional hierarchical frameworks based on MoS₂ nanosheets self-assembled on graphene oxide for efficient electrocatalytic hydrogen evolution. *ACS Appl. Mater. Interfaces* **6**(23), 21534–21540 (2014). <https://doi.org/10.1021/am506545g>
20. S. Linic, P. Christopher, D.B. Ingram, Plasmonic-metal nanostructures for efficient conversion of solar to chemical energy. *Nat. Mater.* **10**, 911–921 (2011). <https://doi.org/10.1038/nmat3151>
21. S. Zu, B. Li, Y. Gong, Z. Li, P.M. Ajayan, Z. Fang, Active control of plasmon–exciton coupling in MoS₂–Ag hybrid nanostructures. *Adv. Opt. Mater.* **4**(10), 1463–1469 (2016). <https://doi.org/10.1002/adom.201600188>
22. A. Ali, F.A. Mangrío, X. Chen, Y. Dai, K. Chen et al., Ultrathin MoS₂ nanosheets for high-performance photoelectrochemical applications via plasmonic coupling with Au nanocrystals. *Nanoscale* **11**(16), 7813–7824 (2019). <https://doi.org/10.1039/C8NR10320H>
23. Y. Shi, J. Wang, C. Wang, T.-T. Zhai, W.-J. Bao et al., Hot electron of Au nanorods activates the electrocatalysis of hydrogen evolution on MoS₂ nanosheets. *J. Am. Chem. Soc.* **137**(23), 7365–7370 (2015). <https://doi.org/10.1021/jacs.5b01732>
24. Y. Kang, S. Najmaei, Z. Liu, Y. Bao, Y. Wang et al., Plasmonic hot electron induced structural phase transition in a MoS₂ monolayer. *Adv. Mater.* **26**(37), 6467–6471 (2014). <https://doi.org/10.1002/adma.201401802>
25. Y.H. Chiu, S.B. Naghadeh, S.A. Lindley, T.H. Lai, M.Y. Kuo et al., Yolk–shell nanostructures as an emerging photocatalyst paradigm for solar hydrogen generation. *Nano Energy* **62**, 289–298 (2019). <https://doi.org/10.1016/j.nanoen.2019.05.008>
26. Y.H. Chiu, K.D. Chang, Y.J. Hsu, Plasmon-mediated charge dynamics and photoactivity enhancement for Au-decorated ZnO nanocrystals. *J. Mater. Chem. A* **6**(10), 4286–4296 (2018). <https://doi.org/10.1039/C7TA08543E>
27. J.M. Li, H.Y. Cheng, Y.H. Chiu, Y.J. Hsu, ZnO–Au–SnO₂ Z-scheme photoanodes for remarkable photoelectrochemical water splitting. *Nanoscale* **8**(34), 15720–15729 (2016). <https://doi.org/10.1039/C6NR05605A>
28. Y.L. Huang, W.S. Chang, C.N. Van, H.J. Liu, K.A. Tsai et al., Tunable photoelectrochemical performance of Au/BiFeO₃ heterostructure. *Nanoscale* **8**(34), 15795–15801 (2016). <https://doi.org/10.1039/C6NR04997D>
29. C.N. Van, W.S. Chang, J.W. Chen, K.A. Tsai, W.Y. Tzeng et al., Heteroepitaxial approach to explore charge dynamics across Au/BiVO₄ interface for photoactivity enhancement. *Nano Energy* **15**, 625–633 (2015). <https://doi.org/10.1016/j.nanoen.2015.05.024>
30. Y.C. Chen, T.C. Liu, Y.J. Hsu, ZnSe-0.5N₂H₄ hybrid nanostructures: a promising alternative photocatalyst for solar conversion. *ACS Appl. Mater. Interfaces* **7**(3), 1616–1623 (2015). <https://doi.org/10.1021/am507085u>

31. Y.C. Pu, G. Wang, K.D. Chang, Y. Ling, Y.K. Lin et al., Au nanostructure-decorated TiO₂ nanowires exhibiting photoactivity across entire UV–visible region for photoelectrochemical water splitting. *Nano Lett.* **13**(8), 3817–3823 (2013). <https://doi.org/10.1021/nl4018385>
32. K.H. Chen, Y.C. Pu, K.D. Chang, Y.F. Liang, C.M. Liu et al., Ag-nanoparticle-decorated SiO₂ nanospheres exhibiting remarkable plasmon-mediated photocatalytic properties. *J. Phys. Chem. C* **116**(35), 19039–19045 (2012). <https://doi.org/10.1021/jp306555j>
33. Y.Y. Li, J.H. Wang, Z.J. Luo, K. Chen, Z.Q. Cheng et al., Plasmon-enhanced photoelectrochemical current and hydrogen production of (MoS₂–TiO₂)/Au hybrids. *Sci. Rep.* **7**, 7178 (2017). <https://doi.org/10.1038/s41598-017-07601-1>
34. L.V. Nang, E.T. Kim, Controllable synthesis of high-quality graphene using inductively-coupled plasma chemical vapor deposition. *J. Electrochem. Soc.* **159**(4), K93–K96 (2012). <https://doi.org/10.1149/2.082204jes>
35. J. Jeon, S.K. Jang, S.M. Jeon, G. Yoo, Y.H. Jang, J.-H. Park, S. Lee, Layer-controlled CVD growth of large-area two-dimensional MoS₂ films. *Nanoscale* **7**(5), 1688–1695 (2015). <https://doi.org/10.1039/C4NR04532G>
36. C. Yim, M. O'Brien, N. McEvoy, S. Winters, I. Mirza, J.G. Lunney, G.S. Duesberg, Investigation of the optical properties of MoS₂ thin films using spectroscopic ellipsometry. *Appl. Phys. Lett.* **104**(10), 103114 (2014). <https://doi.org/10.1063/1.4868108>
37. L. Bai, X. Cai, J. Lu, L. Li, S. Zhong et al., Surface and interface engineering in Ag₂S@MoS₂ core–shell nanowire heterojunctions for enhanced visible photocatalytic hydrogen production. *ChemCatChem* **10**(9), 2107–2114 (2018). <https://doi.org/10.1002/cctc.201701998>
38. P. Zuo, L. Jiang, X. Li, B. Li, P. Ran et al., Metal (Ag, Pt)–MoS₂ hybrids greenly prepared through photochemical reduction of femtosecond laser pulses for SERS and HER. *ACS Sustain. Chem. Eng.* **6**(6), 7704–7714 (2018). <https://doi.org/10.1021/acssuschemeng.8b00579>
39. J. Zhu, Z. Wang, H. Yu, N. Li, J. Zhang et al., Argon plasma induced phase transition in monolayer MoS₂. *J. Am. Chem. Soc.* **139**(30), 10216–10219 (2017). <https://doi.org/10.1021/jacs.7b05765>
40. J.D. Major, M. Al Turkestani, L. Bowen, M. Brossard, C. Li et al., In-depth analysis of chloride treatments for thin-film CdTe solar cells. *Nat. Commun.* **7**, 13231 (2016). <https://doi.org/10.1038/ncomms13231>
41. G. Eda, H. Yamaguchi, D. Voiry, T. Fujita, M. Chen, M. Chhowalla, Photoluminescence from chemically exfoliated MoS₂. *Nano Lett.* **11**(12), 5111–5116 (2011). <https://doi.org/10.1021/nl201874w>
42. W.H. Lin, Y.H. Chiu, P.W. Shao, Y.J. Hsu, Metal-particle-decorated ZnO nanocrystals: photocatalysis and charge dynamics. *ACS Appl. Mater. Interfaces* **8**(48), 32754–32763 (2016). <https://doi.org/10.1021/acsami.6b08132>
43. Y.C. Chen, Y.C. Pu, Y.J. Hsu, Interfacial charge carrier dynamics of the three-component In₂O₃–TiO₂–Pt heterojunction system. *J. Phys. Chem. C* **116**(4), 2967–2975 (2012). <https://doi.org/10.1021/jp210033y>
44. M. Jalali, R.S. Moakhar, T. Abdelfattah, E. Filine, S.S. Mahshid, S. Mahshid, Nanopattern-assisted direct growth of peony-like 3D MoS₂/Au composite for nonenzymatic photoelectrochemical sensing. *ACS Appl. Mater. Interfaces* **12**(6), 7411–7422 (2020). <https://doi.org/10.1021/acsami.9b17449>
45. K.K. Patra, C.S. Gopinath, Bimetallic and plasmonic Ag–Au on TiO₂ for solar water splitting: an active nanocomposite for entire visible-light-region absorption. *ChemCatChem* **8**(20), 3294–3301 (2016). <https://doi.org/10.1002/cctc.201600937>
46. C. Burda, X. Chen, R. Narayanan, M.A. El-Sayed, Chemistry and properties of nanocrystals of different shapes. *Chem. Rev.* **105**(4), 1025–1102 (2005). <https://doi.org/10.1021/cr030063a>
47. H. Lee, S. Deshmukh, J. Wen, V.Z. Costa, J.S. Schuder et al., Layer-dependent interfacial transport and optoelectrical properties of MoS₂ on ultraflat metals. *ACS Appl. Mater. Interfaces* **11**(34), 31543–31550 (2019). <https://doi.org/10.1021/acsami.9b09868>
48. Y.J. Yu, Y. Zhao, S. Ryu, L.E. Brus, K.S. Kim, P. Kim, Tuning the graphene work function by electric field effect. *Nano Lett.* **9**(10), 3430–3434 (2009). <https://doi.org/10.1021/nl901572a>
49. D. Cao, W. Luo, J. Feng, X. Zhao, Z. Lia, Z. Zou, Cathodic shift of onset potential for water oxidation on a Ti⁴⁺ doped Fe₂O₃ photoanode by suppressing the back reaction. *Energy Environ. Sci.* **7**(2), 752–759 (2014). <https://doi.org/10.1039/C3EE42722F>
50. S.U.M. Khan, M. Al-Shahry, W.B. Ingler Jr., Efficient photochemical water splitting by a chemically modified n-TiO₂. *Science* **297**(5590), 2243–2245 (2002). <https://doi.org/10.1126/science.1075035>
51. X. Xu, G. Zhou, X. Dong, J. Hu, Interface band engineering charge transfer for 3D MoS₂ photoanode to boost photoelectrochemical water splitting. *ACS Sustain. Chem. Eng.* **5**(5), 3829–3836 (2017). <https://doi.org/10.1021/acssuschemeng.6b02883>
52. Y. Pi, Z. Li, D. Xu, J. Liu, Y. Li et al., 1T-phase MoS₂ nanosheets on TiO₂ nanorod arrays: 3D photoanode with extraordinary catalytic performance. *ACS Sustain. Chem. Eng.* **5**(6), 5175–5182 (2017). <https://doi.org/10.1021/acssuschemeng.7b00518>
53. Q. Pan, C. Zhang, Y. Xiong, Q. Mi, D. Li et al., Boosting charge separation and transfer by plasmon-enhanced MoS₂/BiVO₄ p–n heterojunction composite for efficient photoelectrochemical water splitting. *ACS Sustain. Chem. Eng.* **6**(5), 6378–6387 (2018). <https://doi.org/10.1021/acssuschemeng.8b00170>
54. L. Zeng, X. Li, S. Fan, M. Zhang, Z. Yin, M. Tadé, S. Liu, Photo-driven bioelectrochemical photocathode with polydopamine-coated TiO₂ nanotubes for self-sustaining MoS₂ synthesis to facilitate hydrogen evolution. *J. Power Sources* **413**, 310–317 (2019). <https://doi.org/10.1016/j.jpowsour.2018.12.054>



-
55. S.J.A. Moniz, S.A. Shevlin, D.J. Martin, Z.-X. Guo, J. Tang, Visible-light driven heterojunction photocatalysts for water splitting—a critical review. *Energy Environ. Sci.* **8**(3), 731–759 (2015). <https://doi.org/10.1039/C4EE03271C>
56. C. Jiang, S.J.A. Moniz, A. Wang, T. Zhang, J. Tang, Photoelectrochemical devices for solar water splitting—materials and challenges. *Chem. Soc. Rev.* **46**(15), 4645–4660 (2017). <https://doi.org/10.1039/C6CS00306K>